Materials Advances

ROYAL SOCIETY OF CHEMISTRY

PAPER

View Article Online
View Journal | View Issue

Cite this: *Mater. Adv.*, 2024, 5, 2057

Multistep transitions in spin crossover materials without long-range spin state order from dimensional reduction

Gian Ruzzi, [a] Jace Cruddas [b] and Benjamin J. Powell *[a]

Received 29th November 2023,
Accepted 14th January 2024

DOI: 10.1039/d3ma01057k

rsc.li/materials-advances

Most theories of multistep spin crossover (SCO) have focused on intermediate phases with long-range spin state order. However, disordered intermediate phases have also been observed experimentally. Here we show that the interplay of crystallographically inequivalent SCO centres with elastic interactions between SCO centres can lead to an effective reduction in the dimensionality of the system. This is highly analogous to dimensional reduction in quantum magnetism. The resulting quasi-one-dimensional and quasi-zero-dimensional models naturally result in disorder at non-zero temperatures, explaining the absence of long-range spin state order in our calculations. Furthermore, the low effective dimensionality can strongly suppress short-range correlations and hence diffuse scattering should not necessarily be expected to be observed experimentally in these disordered phases. Our model contains parameter regimes where disordered intermediate phases give rise to diffuse scattering and other regimes where disordered intermediate phases do not. Our results are in good agreement with experiments on $[Fe^{II}_3(saltrz)_6(M^{II}(CN)_4)_3]\cdot 8(H_2O)$ [Sciortino *et al.*, *Chem. Sci.*, 2017, **8**, 701].

1 Introduction

Disorder is crucial for the (potential) uses of many materials including photovoltaics (hybrid organic–inorganic perovskites), ferroelectrics (*e.g.*, $BaTiO_3$), and magnets (spinels).[1] Further applications are being actively investigated,[1] therefore a key goal is to identify new routes to disordered materials that provide resources for future potential applications.

Disorder does not imply that the system is completely random. Typically, short-range correlations remain between the low-energy degrees of freedom in disordered materials.[1] A classic example is the ice rules in water ice, which dictate the local properties of oxygen–hydrogen bonds. As an extremely large (macroscopic) number of micro-states are consistent with the ice rules, the instantaneous configurations are random on large length-scales. Nevertheless the ice-rules enforce strong short-range correlations. This results in diffuse scattering in diffraction experiments on water ice.[2] Analogous ice rules give rise to a distinctive pattern of diffuse scattering, known as 'pinch points', in spin ices (magnetic analogues of water ice).[3–5] In general, diffuse scattering is a powerful experimental signature of the short-range correlations expected in disordered phases.

Recently, several possible disordered phases of spin crossover (SCO) materials have been discussed theoretically, including spin state ice,[6] Coulomb phases,[7] spin state glasses,[8] and spin state smectics.[9] Distinctive diffuse scattering signatures are predicted for these phases. Contemporaneously, several SCO materials with significant disorder have been identified experimentally.[10–17] However, to date connections between theories of and experiments on disordered SCO phases remain weak, leaving a far from complete understanding of disordered phases in SCO materials.

SCO materials contain metal centres that can take two different electronic configurations: high spin (HS) and low spin (LS). For a solution of equivalent molecules, this results in a crossover from majority HS at high temperatures to majority LS at low temperatures. This is driven by the free energy difference between HS and LS molecules, $\Delta G = G_H - G_L = \Delta H - T\Delta S$, where $\Delta H = H_H - H_L$ is the enthalpy difference, and $\Delta S = S_H - S_L$ is the entropy difference, and the subscripts H and L label the properties of HS and LS SCO centres respectively. Thus, we expect equal numbers of HS and LS SCO centres at the temperature $T_{1/2} = \Delta H/\Delta S$.

However, in the solid state the behaviour of SCO materials can be significantly richer. Firstly, elastic interactions between SCO centres can drive the spin crossover into a true thermodynamic phase transition between HS and LS phases. This phase transition is typically first order and therefore hysteretic. Secondly, intermediate phases are found in many SCO materials. Typically, these correspond to ordered states with repeating

[a] *School of Mathematics and Physics, The University of Queensland, QLD 4072, Australia. E-mail: powell@physics.uq.edu.au*
[b] *School of Psychological Sciences, Monash University, 770 Blackburn Road, Clayton VIC 3168, Australia*

patterns of HS and LS molecules, that are highly analogous to antiferromagnetism.[18,19]

The two most discussed causes of intermediate phases are: (i) elastic interactions;[19,20] and (ii) crystallographic inequivalency of SCO centres.[21] Elastic interactions tend to favour near neighbours with opposite spin states.[6,20] Thus, when ΔG is small, *i.e.*, for temperatures near $T_{1/2}$, elastic interactions can stabilise a phase with an alternating pattern of HS and LS molecules, for example, a chequerboard or stripe pattern.[16,19,20,22–50] This leads to a two-step transition, with three plateaus observed in χT corresponding to HS fractions, γ_{HS}, of 0, 1/2, and 1, where χ is the magnetic susceptibility. Complicated interactions can lead to more complex intermediate spin state orders and hence more intermediate steps.[11,16,19,24–28,31,33,39,50–55] Crystallographically inequivalent SCO centres can also lead to multi-step crossovers, with the inequivalent sets of sites changing spin states at different temperatures.[21] For example, a simple model of this is to assign different ΔG to inequivalent sites.

Both of these mechanisms lead to intermediate states with an ordered pattern of HS and LS SCO centres. If all SCO centres are equivalent and interactions drive long-range spin state order, then this spontaneously breaks a crystallographic symmetry. However, if the pattern of crystallographically inequivalent centres pre-exists at high temperatures, then long range spin state ordering does not require any symmetry breaking (as the relevant symmetry is absent at high temperatures).

Many materials have both significant elastic interactions and crystallographically inequivalent SCO centres. However, this has been less well explored theoretically.[21]

Recently, $[Fe^{II}_3(saltrz)_6(M^{II}(CN)_4)_3]\cdot 8(H_2O)$, where M^{II} = Pd or Pt, and saltrz = (*E*)-2-((((4*H*-1,2,4-triazol-4-yl)imino)methyl)phenol), have been shown to undergo four-step SCO transitions with hysteresis loops around the intermediate plateaus.[16] The plateaus are not very flat suggesting significant disorder in the arrangements of spin states. More direct evidence for disordered spin states comes from X-ray crystallography.[16] However, puzzlingly, no diffuse scattering was observed.[56]

Here we demonstrate that competition between elastic interactions and variations in the local physics of the SCO centres due to crystallographic inequivalency can lead to an effective theory with lower dimensionality than the full crystal. This has important experimental consequences, particularly for understanding X-ray scattering experiments. We find that the quasi-two-dimensional model we study can be reduced to either an effective quasi-one-dimensional (q1d) model or an effective quasi-zero-dimensional (q0d) model in different intermediate plateaus. This reduced dimensionality leads to disordered phases and hence intermediate plateaus in γ_{HS} without long-range spin state order. Furthermore, the reduced dimensionality also suppresses short-range spin state order, and therefore diffuse scatter. We show that this scenario explains the observed[16] SCO transitions in $[Fe^{II}_3(saltrz)_6(M^{II}(CN)_4)_3]\cdot 8(H_2O)$ and that the absence of diffuse scatter is because the short-range correlations are extremely weak.

Finally, we discuss how stronger short range correlations can emerge from effective q1d theories and predict the diffuse scattering pattern that would be expected in this case. We show that short-range spin state correlations without long-range spin state order could explain the observed[17] diffuse scattering from three analogous 1D polymeric Fe(II) SCO materials that contain the ligand 4,6-bis(2′,2″-pyridyl)pyrazine.

2 Elastic and Ising-like models of $[Fe^{II}_3(saltrz)_6(M^{II}(CN)_4)_3]\cdot 8(H_2O)$

The SCO active Fe sites in $[Fe^{II}_3(saltrz)_6(M^{II}(CN)_4)_3]\cdot 8(H_2O)$ form quasi-two-dimensional square lattices with covalently bonded networks connecting the Fe ions along the diagonal of the squares (illustrated by the grey lines in Fig. 1). Weaker interlayer elastic interactions arise from the interdigitated saltrz ligands.[16] At high and low temperatures, the unit cell is composed of two unique Fe(II) sites, labelled Fe1 and Fe2. At intermediate (*ca.* 150–195 K) temperatures two distinct species of Fe1 and Fe2 sites are observed (labelled Fe1a, Fe1b, Fe2a and Fe2b). The distribution of crystallographically distinct Fe sites is illustrated in Fig. 1.

Therefore, we consider a square lattice of SCO centres coupled by springs, sketched in Fig. 1, and described by the Hamiltonian[6,19]

$$H=\frac{1}{2}\sum_i(\Delta H_i - T\Delta S_i)\sigma_i+\sum_{n=1}^{5}\frac{k_n}{2}\sum_{\langle i,j\rangle_n}\left\{|\mathbf{r}_{i,j}|-\eta_n\left[\overline{R}+\delta\left(\sigma_i+\sigma_j\right)\right]\right\}^2 \quad (1)$$

with periodic boundary conditions, where the pseudospin degrees of freedom are $\sigma_i = 1$ (-1) if the ith SCO centre is HS (LS), $\langle i,j\rangle_n$ indicates that the sum runs over all nth nearest neighbours, ΔH_i is the enthalpy difference between the HS and LS states of the ith SCO centre, ΔS_i is the entropy difference between the HS and LS states of the ith SCO centre, k_n is the

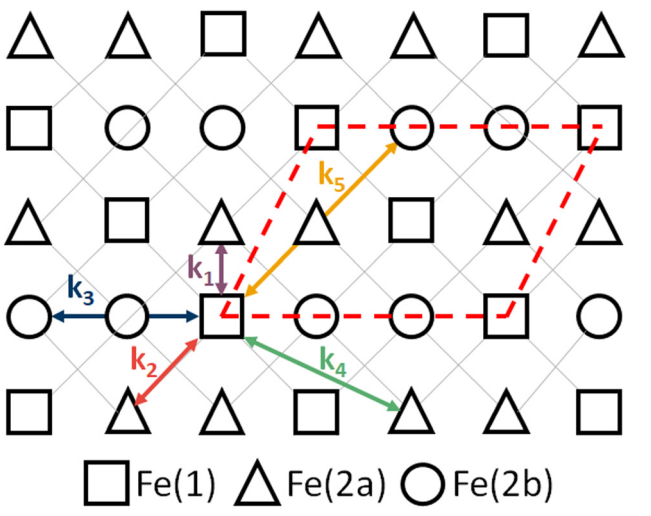

Fig. 1 Sketch of the model studied here (eqn (1)). The nth nearest neighbours interactions, k_n, are marked. The pattern of Fe1, Fe2a and Fe2b sites is that found in a single layer of $[Fe^{II}_3(saltrz)_6(M^{II}(CN)_4)_3]\cdot 8(H_2O)$. The dashed red parallelogram indicates the primitive unit cell.

spring constant between nth nearest neighbours, $|\mathbf{r}_{i,j}|$ is the instantaneous distance between sites i and j, $\eta_n = 1, \sqrt{2}, 2, \sqrt{5}, 2\sqrt{2}, \ldots$ is the ratio of distances between the nth and 1st nearest-neighbour distance on the undistorted square lattice, $\bar{R} = (R_{HS} + R_{LS})/2$, and $\delta = (R_{HS} - R_{LS})/4$, R_{HS} (R_{LS}) is the average distance between the centres of nearest neighbour SCO centres in the HS (LS) phase.

Motivated by the pattern of Fe1, Fe2a and Fe2b sites observed in $[Fe_3^{II}(saltrz)_6(M^{II}(CN)_4)_3]\cdot 8(H_2O)$,[16] we consider three crystallographically distinct metal centres in the pattern shown in Fig. 1. For simplicity we neglect the differences between Fe1a and Fe1b sites found at intermediate temperatures,[16] as the spin state is always the same for these two types of metal centre; and set $\Delta S_i = \Delta S$ on all sites, encapsulating the differences between sites solely *via* ΔH_i.

We only consider up to fifth nearest neighbor interactions. Therefore, we do not seek to fit every detail of the experiments on $[Fe_3^{II}(saltrz)_6(M^{II}(CN)_4)_3]\cdot 8(H_2O)$, and limit ourselves to reproducing the key qualitative features. For metal centres joined by networks of covalent bonds one expects k to be large and positive, as the metal–metal separation should be close to the minimum of the potential,[6,19] for our model these interactions are k_2 and k_5, see Fig. 1. For weak through space interactions, as is the case for k_1, k_3, and k_4 (Fig. 1), one typically expects metal–metal separations that are larger than the distance for the minimum of the interaction potential. This leads to negative spring constants.[6,19] Therefore, one expects $k < 0$ for many materials.[19] This has profound consequences for the long range spin state order observed in different materials. In Section 3.1 we set $k_1 > 0$, $k_2 = 0.48|k_1|$, $k_3 = -0.23|k_1|/2$, $k_4 = 0$, and $k_5 = 0.09|k_1|$ to model $[Fe_3^{II}(saltrz)_6(M^{II}(CN)_4)_3]\cdot 8(H_2O)$. In Section 3.2 we briefly discuss the effects of varying these parameters, particularly setting $k_1 < 0$.

We make the symmetric breathing mode approximation (SBMA).[6,19] That is, we assume that the topology of the lattice is not altered by the changes in the spin states, and that the distance between any pair of nearest neighbors is $r_{i,j} = R$; we variationally minimize R. In this approximation Hamiltonian (1) becomes an Ising–Husimi–Temperley model in a longitudinal field:[6]

$$H \approx \sum_{n=1}^{5} J_n \sum_{\langle i,j\rangle_n} \sigma_i\sigma_j - \frac{J_\infty}{N}\sum_{i,j}\sigma_i\sigma_j + \frac{1}{2}\sum_i \Delta G_i\sigma_i, \qquad (2)$$

where, $J_n = k_n{\eta_n}^2\delta^2$ is the pseudospin–pseudospin interaction between the nth nearest-neighbors, $J_\infty = \delta^2\sum_{n=1}^{m}\left(k_n z_n {\eta_n}^2\right)$ is the strain, $\Delta G_i = \Delta H_i - T\Delta S_i$ is the free energy difference between the HS and LS states of the ith SCO centre, z_n is the coordination number for nth nearest neighbors and N is the number of metal sites.

Although, the spring constants will often be negative for through space interactions,[19] the possible range of spring constants is constrained by the fact that the lattice described by Hamiltonian (1) must be stable. Thus, we must have $\partial^2 H/\partial R^2 = J_\infty/\delta^2 > 0$.

We solve the Ising-Husimi-Temperley model (eqn (2)) *via* Metropolis Monte Carlo simulations on a $N = 60 \times 60$ site lattice. Cooling (heating) runs are initiated with all metals in the HS (LS) state at the highest (lowest) temperature studied and the temperature is lowered (raised) in steps of $0.025|k_1|\delta^2/k_B$. In each case the system is equilibrated for $4000N$ Monte Carlo steps and measurements are taken for $40\,000N$ steps.

2.1 Sum rule for the structure factor

The pseudospin structure factor,

$$S(\boldsymbol{q}) = \frac{1}{N}\sum_{i,j}\langle\sigma_i\sigma_j\rangle e^{-i\boldsymbol{q}\cdot\mathbf{r}_{i,j}}, \qquad (3)$$

obeys the sum rule[57]

$$\lim_{N_q\to\infty}\frac{1}{N}\sum_{\boldsymbol{q}\in BZ} S(\boldsymbol{q}) = \frac{R^2}{4\pi^2}\int_{BZ} d^2\boldsymbol{q}\, S(\boldsymbol{q}) = 1 \qquad (4)$$

where N is the number of Fe sites in the real space lattice and N_q is the number of q points. This is a powerful tool that allows us to distinguish between the contributions to the sum from regions around the Bragg peaks and the background. To do this we calculate the average structure factor evaluated over 2000 configurations, each separated by $20N$ Monte Carlo steps, during a cooling/heating calculation and performed the $\boldsymbol{q}$-integrals numerically on a 61×61 Monkhorst–Pack grid.[58]

3 Results

3.1 Reduced dimensionality and disordered intermediate plateaus

To understand the interplay between elastic interactions and multiple Fe species it is helpful to first consider what we would expect if there were no interactions between SCO centres (*i.e.*, for all $k_N = 0$). First let us consider $\Delta H_1 \ll \Delta H_{2a} = \Delta H_{2b} \equiv \Delta H_2$, which means Fe2a and Fe2b sites are equivalent to one another but distinct from the Fe1 sites. This, gives a two step crossover, Fig. 2a. On heating from low temperatures, the first step occurs at $T_{1/6} = \Delta H_1/\Delta S$, where the Fe1 sites have a 50% probability of being HS and the Fe2a and Fe2b are almost all LS.† As there are twice as many Fe2 sites as Fe1 sites (see Fig. 2) the total fraction of HS metals is $\gamma_{HS} \simeq 1/6$ at $T = T_{1/6}$. The second step occurs at $T_{2/3} = \Delta H_2/\Delta S$, where the Fe2 sites to have a 50% probability of being HS and almost all of the Fe1 sites are HS. Thus, $\gamma_{HS} \simeq 2/3$ at $T = T_{2/3}$.

For $\Delta H_1 \ll \Delta H_{2b} \ll \Delta H_{2a}$ we expect a three step crossover, Fig. 1b. Again, the first step occurs at $T_{1/6} = \Delta H_1/\Delta S$ where $\gamma_{HS} = 1/6$. But now, the second step occurs at $T_{1/2} = \Delta H_{2b}/\Delta S$, where one expects the Fe2b sites to have a 50% probability of being HS, almost all of the Fe1 sites are HS, and almost all of the Fe2a are LS, as such $\gamma_{HS} = 1/2$. The third step occurs at $T_{5/6} = \Delta H_{2a}/\Delta S$, where one expects the Fe2a sites to have a 50% probability of being HS, whereas almost all of the Fe1 and Fe2b sites are HS, therefore $\gamma_{HS} = 5/6$.

† They are strictly all LS in the limit $\Delta H_2 \to \infty$.

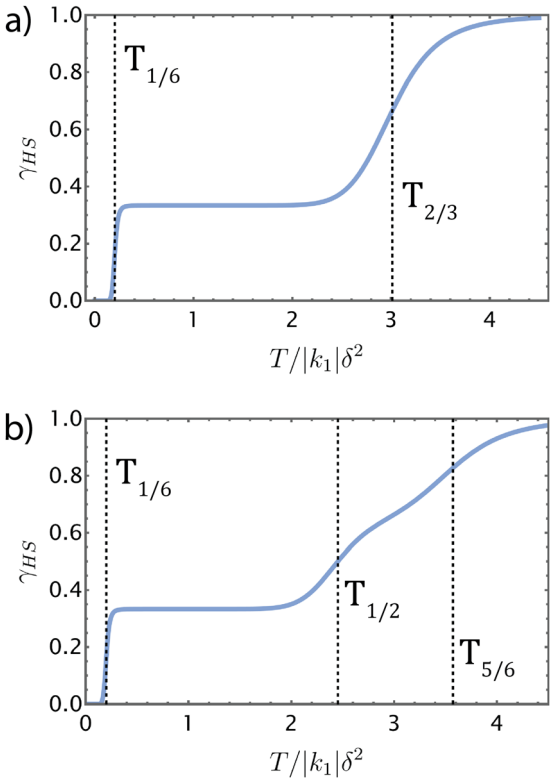

Fig. 2 Spin crossover for inequivalent sites without interactions. (a) Results for Fe2a and Fe2b sites equivalent to each other but inequivalent from Fe1 sites $(\Delta H_1 = \overline{\Delta H} - \delta H_1,\ \Delta H_{2a} = \overline{\Delta H} + \delta H_1$ and $\Delta H_{2b} = \overline{\Delta H} + \delta H_1)$; and (b) Fe1, Fe2a and Fe2b sites all inequivalent $(\Delta H_1 = \overline{\Delta H} - \delta H_1,\ \Delta H_{2a} = \overline{\Delta H} + \delta H_1 + \delta H_2$ and $\Delta H_{2b} = \overline{\Delta H} + \delta H_1 - \delta H_2)$. In all panels ΔS = 4ln(5)k_B, $\overline{\Delta H} = 10.35|k_1|\delta^2$, δH_1 = $9.05|k_1|\delta^2$, δH_2 = $3.6|k_1|\delta^2$, and k_n = 0 for all n.

Elastic interactions significantly change the temperature dependence of the HS fraction. We show calculations for three different patterns of inequivalent Fe ions with the same elastic interactions and ΔS in Fig. 3. It is immediately clear that the inequivalent sites cause dramatic changes in the behaviour of the model and that the elastic interactions cause dramatic differences from the non-interacting model. Thus, the interplay of the pattern of inequivalent sites and elastic interactions is crucial for understanding this behaviour – neither can explain the physics alone.

When all Fe sites are equivalent ($\Delta H_1 = \Delta H_{2b} = \Delta H_{2a}$; Fig. 3a) we see a one step transition for the heating run (all sites were initialized in the LS state), and no transition for the cooling run, *i.e.*, hidden SCO. Thus, interactions have driven the crossover (found without interactions) into a first order phase transition with a very wide hysteresis loop.

When Fe2a and Fe2b sites are equivalent to one another but distinct from Fe1 sites, ($\Delta H_1 < \Delta H_{2b} = \Delta H_{2a}$; Fig. 3b) there is a three step transition with poorly defined intermediate plateaus at γ_{HS} = 1/6 and 2/3. Thus, these plateaus occur around the crossovers expected in the non-interacting model, Fig. 2. This is what one would expect if the interactions stabilised long-range spin state order within one sublattice near the crossovers, *i.e.*, when $\Delta H_i/\Delta S$ is small on the ith sublattice; analogous to

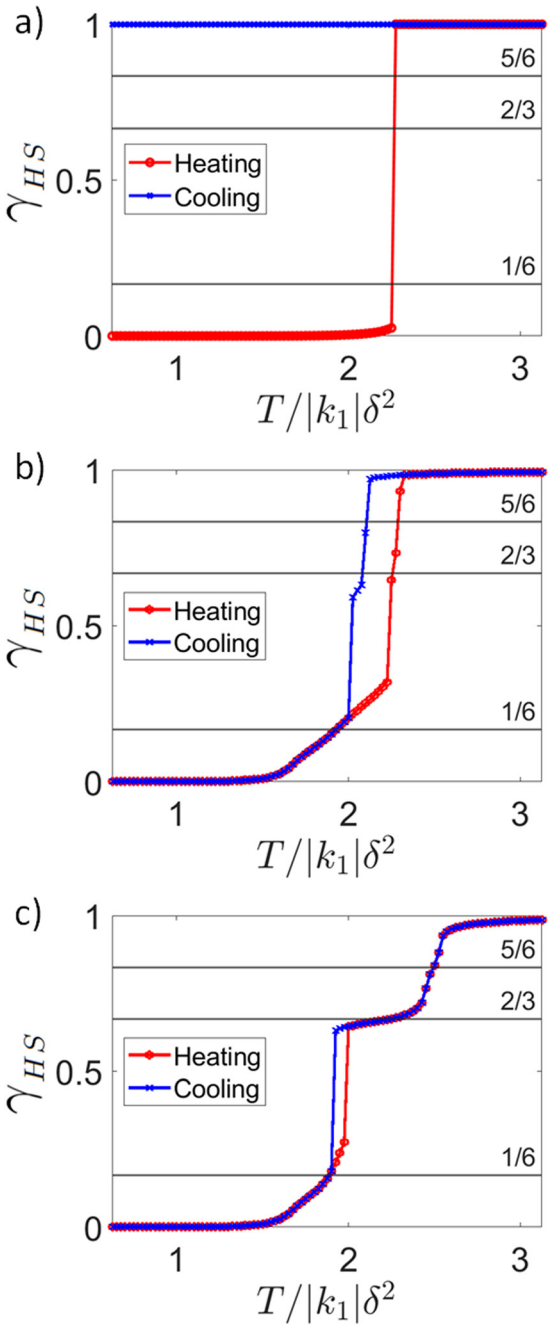

Fig. 3 Changing the inequivalency of the sites while leaving interactions fixed dramatically changes the temperature dependence of HS fraction, γ_{HS}. Here we present calculations with: (a) all Fe sites equivalent $\Delta H_1 = \Delta H_{2a} = \Delta H_{2b} = \overline{\Delta H})$; (b) Fe2a and Fe2b sites equivalent to each other but inequivalent from Fe1 sites $(\Delta H_1 = \overline{\Delta H} - \delta H_1,\ \Delta H_{2a} = \overline{\Delta H} + \delta H_1$ and $\Delta H_{2b} = \overline{\Delta H} + \delta H_1)$; and (c) Fe1, Fe2a and Fe2b sites all inequivalent $(\Delta H_1 = \overline{\Delta H} - \delta H_1,\ \Delta H_{2a} = \overline{\Delta H} + \delta H_1 + \delta H_2$ and $\Delta H_{2b} = \overline{\Delta H} + \delta H_1 - \delta H_2)$. In all panels ΔS = 4ln(5)k_B, $\overline{\Delta H} = 10.35|k_1|\delta^2$, δH_1 = $9.05|k_1|\delta^2$, δH_2 = $3.6|k_1|\delta^2$, $k_1 > 0$, k_2 = $0.48|k_1|$, k_3 = $-0.23|k_1|$, k_4 = 0, and k_5 = $0.09|k_1|$.

chequerboard or stripe order around $T_{1/2}$ when all Fe's are equivalent. However, we will show below that this is not that case and both of these plateaus are strongly disordered.

When all three Fe sublattices are inequivalent ($\Delta H_1 < \Delta H_{2b} < \Delta H_{2a}$; Fig. 3c) we observe a four step transition with intermediate plateaus at γ_{HS} = 1/6, 2/3, and 5/6. Recall that in the non-interacting model the steps are at γ_{HS} = 1/6, 1/2, and 5/6. Thus, the plateau at γ_{HS} = 1/2 is missing and the γ_{HS} = 2/3 plateau must have a different origin from the other plateaus. Furthermore, the calculated variation of $\gamma_{HS}(T)$ closely resembles the variation of χT with temperature observed in $[Fe_3^{II}(saltrz)_6(M^{II}(CN)_4)_3]\cdot 8(H_2O)$.

In the 1/6 plateaus shown in Fig. 3b and c the Fe2a and Fe2b sites are almost all in the LS state whereas about half of the Fe1 sites are HS (see Fig. 4a for a snapshot). $T_{1/6} \equiv \Delta H_1/\Delta S \simeq 0.202|k_1|\delta^2/k_B$ for the parameters used in Fig. 3. Notice that this temperature is significantly lower than the ranges where the $\gamma_{HS} \simeq 1/6$ plateau is observed ($k_BT/|k_1|\delta^2 \simeq 1.5$–$2.25$ in Fig. 3b, and $k_BT/|k_1|\delta^2 \simeq 1.5$–$2.0$ in Fig. 3c).

To understand this discrepancy we introduce an effective model where all of the Fe2a and Fe2b are constrained to be LS, *i.e.*, we start from the full Hamiltonian (eqn (2)) and set $\sigma_i = -1$ if i is an Fe2a or Fe2b site. This leaves an effective Hamiltonian for the Fe1 sites:

$$H_{1/6} = \frac{1}{2}\left[-8J_1 - 4J_2 - 8J_3 - 8J_4 - 4J_5 + \frac{8}{3}J_\infty + \Delta H_1 - T\Delta S\right] \sum_{i\in \mathrm{Fe1}} \sigma_i + J_2 \sum_{\langle i,j\rangle_2 \in \mathrm{Fe1}} \sigma_i\sigma_j + J_4 \sum_{\langle i,j\rangle_4 \in \mathrm{Fe1}} \sigma_i\sigma_j + J_5 \sum_{\langle i,j\rangle_5 \in \mathrm{Fe1}} \sigma_i\sigma_j - \frac{J_\infty}{N}\sum_{i,j\in \mathrm{Fe1}} \sigma_i\sigma_j, \quad (5)$$

where we have neglected a constant term. This model describes one-dimensional chains running along the diagonals for $\sigma_i \in$ Fe1 [*cf.* Fig. 5e] coupled only by the long-range strain and J_4 (which is zero in our numerical calculations). It is important to notice that the long-range strain couples each pseudospin to all other pseudospins. As such, the long-range strain is only sensitive to the total HS fraction:

$$\frac{J_\infty}{N}\sum_{i,j}\sigma_i\sigma_j = NJ_\infty(2\gamma_{HS} - 1)^2. \quad (6)$$

Therefore, this term cannot stabilise an ordered phase over a disorder phase with the same HS fraction. Thus, the crystallographically distinct Fe sites lead to an effective q1D description of the 2D plane.

The effective q1D model (eqn (5)) predicts that the temperature where we expect half of the Fe1 to be HS is renormalized by the elastic interactions with the LS Fe2a and Fe2b sites to

$$T^*_{1/6} = \frac{8J_\infty/3 - 8J_1 - 4J_2 - 8J_3 - 8J_4 - 4J_5 + \Delta H_1}{\Delta S} = T_{1/6} + \frac{8(k_1 + 5k_2 + 4k_3 + 25k_4 + 20k_5)\delta^2}{3\Delta S}. \quad (7)$$

For the parameters in Fig. 3, $T^*_{1/6} \simeq 1.95|k_1|\delta^2/k_B$, in excellent agreement with the location of the γ_{HS} = 1/6 plateau in our

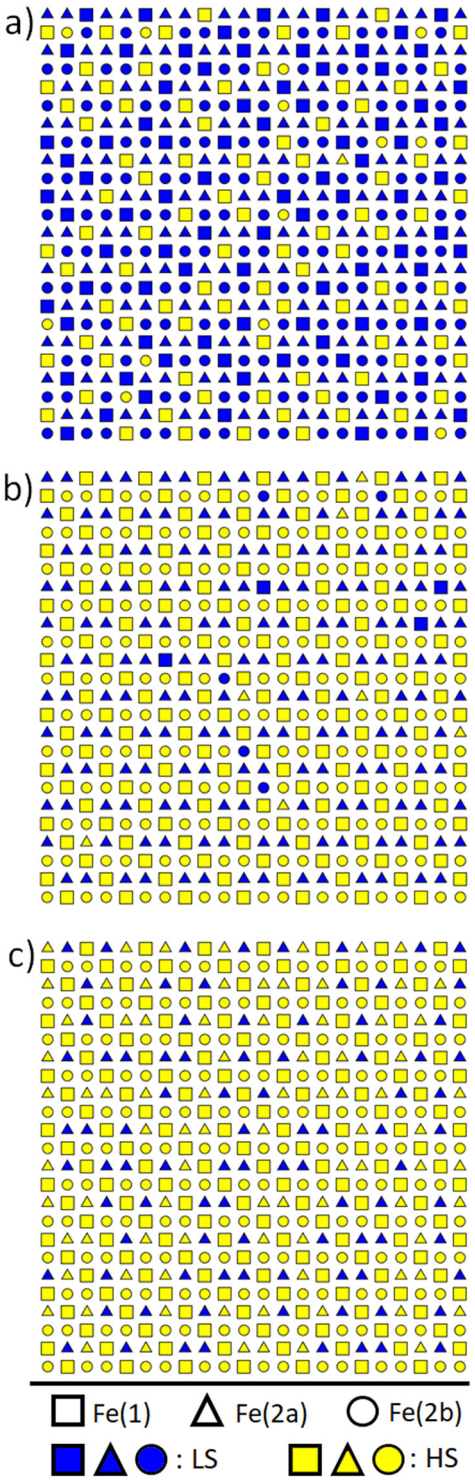

Fig. 4 Snapshots at the three intermediate plateaus in the simulation with Fe1, Fe2a and Fe2b sites all inequivalent (from the simulations shown in Fig. 3c) taken at (a) $T = 1.9|k_1|\delta^2$, (b) $T = 2.25|k_1|\delta^2$, and (c) $T = 2.5|k_1|\delta^2$; corresponding to the plateaus at γ_{HS} = 1/6, 2/3 and 5/6. (a) In the γ_{HS} = 1/6 plateau the Fe2a and Fe2b sites are all LS whereas the Fe1 are disordered and weakly correlated. (b) In the γ_{HS} = 2/3 plateau the Fe1 and Fe2b sites are almost all HS whereas the Fe2a are almost all LS. (c) In the γ_{HS} = 5/6 plateau the Fe1 and Fe2b sites are almost all HS whereas the Fe2a are disordered and weakly correlated. In this figure $\Delta S = 4\ln(5)k_B$, $\Delta H_1 = \overline{\Delta H} - \delta H_1$, $\Delta H_{2a} = \overline{\Delta H} + \delta H_1 + \delta H_2$, $\overline{\Delta H} = 10.35|k_1|\delta^2$, $\delta H_1 = 9.05|k_1|\delta^2$, $\delta H_2 = 3.6|k_1|\delta^2 k_1 > 0$, $k_2 = 0.48|k_1|$, $k_3 = -0.23|k_1|$, $k_4 = 0|k_1|$, and $k_5 = 0.09|k_1|$.

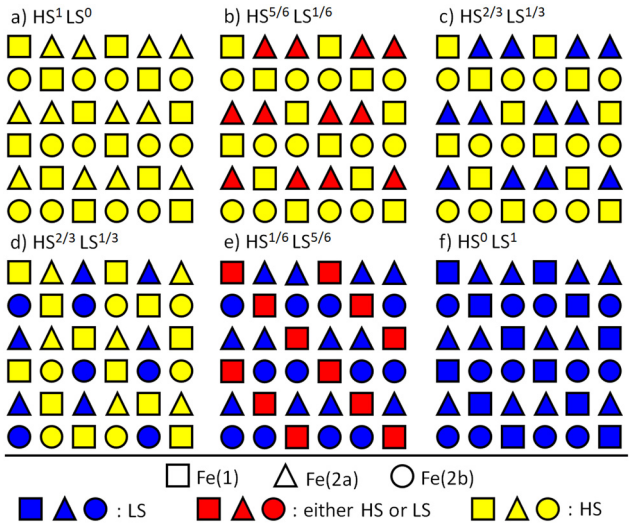

Fig. 5 The key phases discussed in this paper. (a) The HS phase, (b) the γ_{HS} = 5/6 phase. (c) and (d) Two possible states with γ_{HS} = 2/3, (c) is observed when Fe2a and Fe2b are inequivalent. When Fe2a and Fe2b are equivalent a disordered state mixing of (c) and (d) is found. (e) The γ_{HS} = 1/6 phase, the Fe1 sites form decoupled one-dimensional chains, which are disordered at non-zero temperatures. (f) The LS phase.

Monte Carlo simulations. This strongly suggests that in the 1/6-plateau the model has become q1D.

It is well known that there is no long-range order at finite temperature in the one-dimensional Ising model.[59] Therefore, we can test our claim that the q1d model [eqn (5)] describes the 1/6 plateau by more closely examining our Monte Carlo calculations. A typical snapshot is shown in Fig. 4a. It can be clearly seen that nearly all of the Fe2a and Fe2b sites are LS and approximately half of the Fe1 sites are HS, with no apparent spin state order in the spin states of the Fe1s.

This can be made quantitative by calculating the structure factor at $T = T^*_{1/6}$ from our Monte Carlo simulations of the full model (eqn (2)). In an X-ray scatering experiment there is genuine background scatter (from sources unrelated to the spin states of the SCO centres). Therefore, when we discuss diffuse scattering below we will only be interested in clearly defined patterns that could be detected experimentally over the background noise. This, distinction between diffuse scattering and background is, unavoidably, qualitative and somewhat arbitrary. Nevertheless, it is surprising to see that the structure factor, Fig. 6a, shows little sign of structure in the diffuse scattering, even on a logarithmic scale.

To better understand this we analytically calculated the structure factor from the effective q1d model (eqn (5)), Fig. 6d. This closely resembles our Monte Carlo simulation.

To quantify and compare the amount of scattering contributing to the observed peaks in the Monte Carlo and analytical calculations we compute the contributions to the integral $\int S(\boldsymbol{q})\mathrm{d}^2\boldsymbol{q}$ over the first Brillouin zone, of the Bragg peaks enclosed by the black squares in Fig. 6 and the background; the results are shown in Fig. 7a. We find good agreement between both calculations, the only significant difference is that slightly more scattering is present in the background of the Monte Carlo simulation; this is expected as these calculations

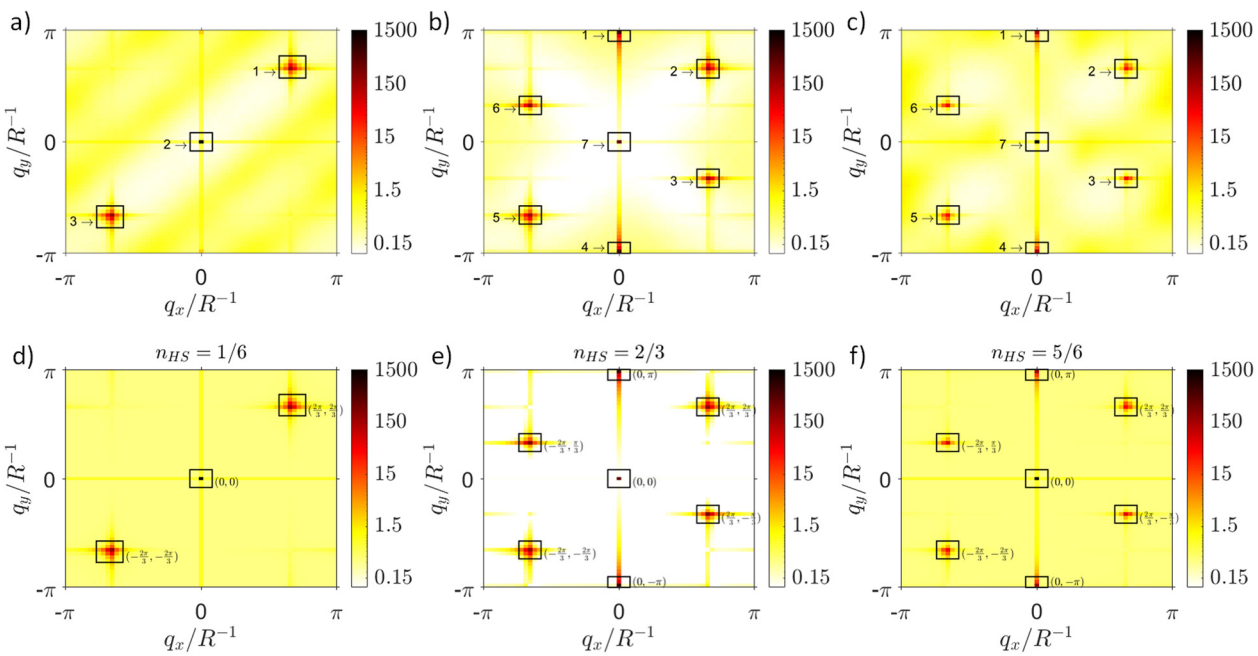

Fig. 6 (top) Structure factors, $S(\boldsymbol{q})$, on a logarithmic scale from the numerical simulations of the 2D model (eqn (2)) shown in Fig. 3c, taken at (a) $T = 1.9|k_1|\delta^2$ (γ_{HS} = 1/6 plateau), (b) $T = 2.25|k_1|\delta^2$ (γ_{HS} = 2/3 plateau), and (c) $T = 2.5|k_1|\delta^2$ (γ_{HS} = 5/6 plateau). The main diffraction peaks are enclosed by black rectangles. (bottom) Normalized structure factors from (d) the effective q1d model (eqn (5)) of the γ_{HS} = 1/6 plateau, (e) the effective q1d zigzag chain model (eqn (9)) of the γ_{HS} = 2/3 plateau, and (f) the effective q0d dimer model (eqn (11)) of the γ_{HS} = 5/6 plateau.

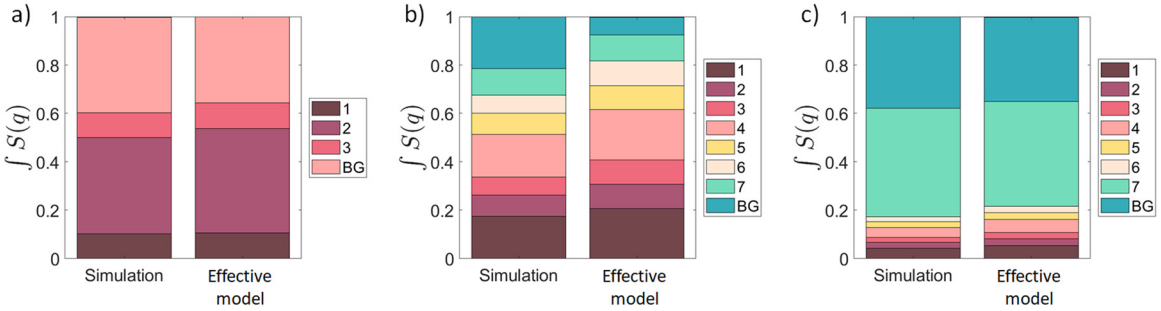

Fig. 7 Bar plots representing the integral over the first Brillouin zone of the structure factors, $\int_{BZ} S(\boldsymbol{q})\mathrm{d}\boldsymbol{q}$, corresponding to the numerical simulation of the 2D model (eqn (2); see Fig. 6a–c) and for the effective models (eqn (5), (9) and (11); see Fig. 6d–f). The plots indicate the portions of the integral corresponding to the Bragg peaks enclosed by rectangles in Fig. 6 and the background (BG). (a) $T = 1.9|k_1|\delta^2$ in the $\gamma_{HS} = 1/6$ plateau, (b) $T = 2.25|k_1|\delta^2$ in the $\gamma_{HS} = 2/3$ plateau, and (c) $T = 2.5|k_1|\delta^2$ in the $\gamma_{HS} = 5/6$ plateau.

are performed at a finite temperature, whereas the analytical calculations are effectively at zero temperature.

Further insight into the lack of diffuse scatter can be gained from the truncated two point spin state correlation function

$$g_{ij} = \langle \sigma_i \sigma_j \rangle - \langle \sigma_i \rangle \langle \sigma_j \rangle. \quad (8)$$

If the sites i and j are uncorrelated then $\langle \sigma_i \sigma_j \rangle = \langle \sigma_i \rangle \langle \sigma_j \rangle$ and $g_{i,j} = 0$. There are weak correlations between Fe1 sites on the same q1d chain, Fig. 8a, and almost no correlations between Fe1 sites in different chains. Similarly there is vanishingly weak correlations between the spin state of Fe1 sites and those of Fe2a and Fe2b sites, Fig. 8b and c. This, together with the above results, strongly support our hypothesis that the material becomes q1d.

The spin state correlation function cannot be directly measured. However, as spin state and atomic position are highly entangled, we expect that the two point spin state correlation function is roughly proportional to the pair-distribution-function (PDF; the equivalent correlation function to that defined in eqn (8) for atomic position instead of spin state). The PDF is directly accessible *via* X-ray scattering and is a standard probe of liquids, glasses, polymers, and other structurally disordered materials.[60] Thus, measurements of the PDF are vital for a deeper understanding of disorder SCO materials.

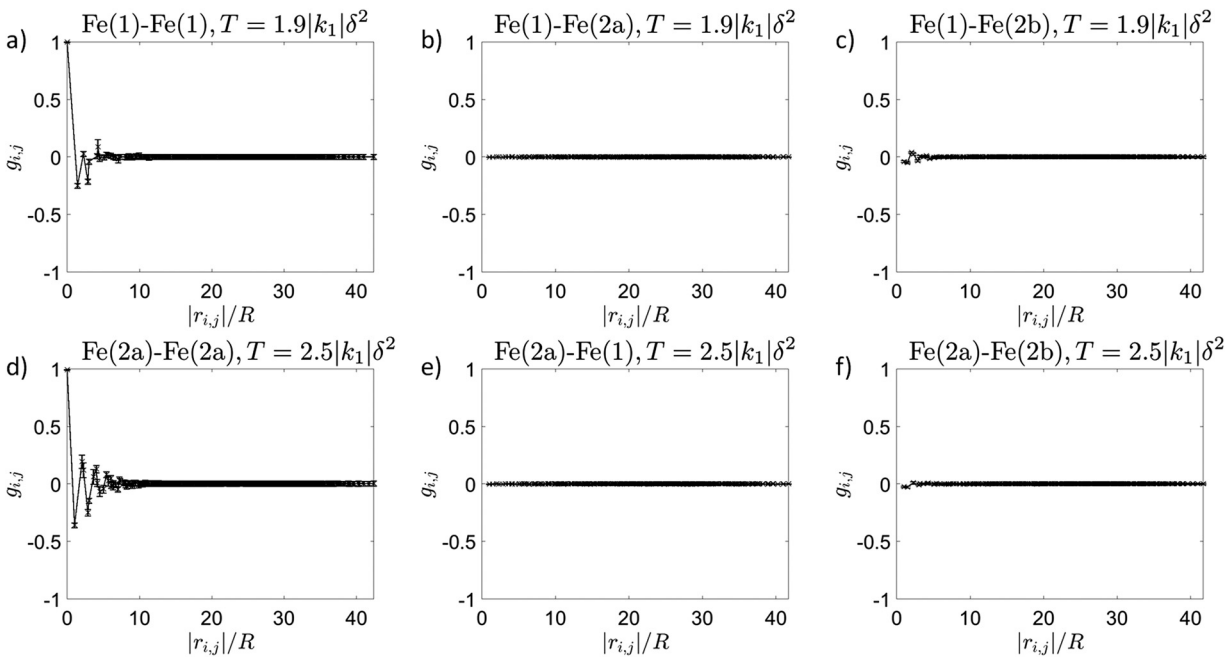

Fig. 8 Two-point spin state correlation function as a function of separation $|r_{i,j}|$ calculated for the simulation depicted in Fig. 3c. (a)–(c) At $T = 1.9|k_1|\delta^2$ in the $\gamma_{HS} = 1/6$ plateau. (d)–(f) At $T = 2.5|k_1|\delta^2$ in the $\gamma_{HS} = 5/6$ plateau. Correlations between (a) Fe1 sites, (b) Fe1 and Fe2a sites, (c) Fe1 and Fe2b sites, (d) Fe2a sites, (e) Fe2a and Fe1 sites, (f) Fe2a and Fe2b sites. For short distances the correlation between Fe1 sites at $T = 1.9|k_1|\delta^2$ are weak, and decay rapidly to zero as the distance increases. Similarly, the correlations between Fe2a at $T = 2.5|k_1|\delta^2$ are weak and decay rapidly to zero as the distance increases. All other correlations are essentially zero. In this figure $\overline{\Delta H} = 10.35|k_1|\delta^2$, $\delta H_1 = 9.05|k_1|\delta^2$, $\delta H_2 = 3.6|k_1|\delta^2$, $k_1 > 0$, $k_2 = 0.48|k_1|$, $k_3 = -0.23|k_1|$, $k_4 = 0|k_1|$, $k_5 = 0.09|k_1|$, and $\Delta S = 4\ln(5)k_B$.

The almost complete absence of correlations between the Fe1 chains and weak short range correlations with chains explain why we find no structured diffuse scatter in the structure factor, Fig. 6a. Experimentally, in the 1/6 plateau we would expect to see a crystal structure showing mixed spin state in the Fe1 sites and no diffuse scattering, which is exactly what was reported for $[Fe^{II}_3(saltrz)_6(M^{II}(CN)_4)_3]\cdot 8(H_2O)$.[16,56]

In the 2/3 plateau with only one type of Fe2 site ($\Delta H_{2a} = \Delta H_{2b} = \Delta H_2$; Fig. 3b) the Fe1 sites are almost all HS. In our Monte Carlo simulations we observe a mixture of the phases depicted in Fig. 5c and d (and states related by symmetry).

To understand the physics of the Fe2 sites it is helpful to consider the case where all of the Fe1 are HS. We can then derive an effective Hamiltonian for the Fe2 sites from the full Hamiltonian (eqn (2)) by setting $\sigma_i = 1$ for all Fe1. This yields

$$\begin{aligned} H_{2/3} &= \frac{1}{2}\left[4J_1 + 2J_2 + 4J_3 + 4J_4 + 2J_5 - \frac{4}{3}J_\infty + \Delta H_2 - T\Delta S\right] \sum_{i\in \mathrm{Fe2}} \sigma_i + J_1 \sum_{\langle i,j\rangle_1 \in \mathrm{Fe2}} \sigma_i\sigma_j + J_2 \sum_{\langle i,j\rangle_2 \in \mathrm{Fe2}} \sigma_i\sigma_j \\ &\quad + J_3 \sum_{\langle i,j\rangle_3 \in \mathrm{Fe2}} \sigma_i\sigma_j + J_4 \sum_{\langle i,j\rangle_4 \in \mathrm{Fe2}} \sigma_i\sigma_j \\ &\quad + J_5 \sum_{\langle i,j\rangle_5 \in \mathrm{Fe2}} \sigma_i\sigma_j - \frac{J_\infty}{N} \sum_{i,j\in \mathrm{Fe2}} \sigma_i\sigma_j. \end{aligned} \tag{9}$$

This model describes zigzag ladders with J_2 along the legs and J_1 along the rungs (plus longer range intra-ladder interactions). However, unlike the effective model of the 1/6 plateau the ladders are coupled standard Ising interactions proportional to (k_3, k_4 and k_5).

The effective model of the 2/3 plateau (eqn (9)) predicts that $T_{2/3}$ is strongly renormalized by the elastic interactions with the HS Fe1 sites, yielding

$$\begin{aligned} T^*_{2/3} &= \frac{4J_1 + 2J_2 + 4J_3 + 4J_4 + 2J_5 - \frac{4}{3}J_\infty + \Delta H_2}{\Delta S} \\ &= T_{2/3} - \frac{4(k_1 + 5k_2 + 4k_3 + 25k_4 + 20k_5)\delta^2}{3\Delta S}. \end{aligned} \tag{10}$$

Thus, the elastic interactions decrease $T_{2/3}$, whereas they increased $T_{1/6}$. For the parameters used in Fig. 3, $T_{2/3} \simeq 3.01|k_1|\delta^2/k_B$ whereas $T^*_{2/3} \simeq 2.14|k_1|\delta^2/k_B$, in good agreement with our Monte Carlo results, Fig. 3b.

As the ladders in the effective model of the $\gamma_{HS} = 2/3$ plateau are coupled by conventional Ising interactions, and not just the long-range strain, which only couples the HS fraction (eqn (6)), the short range correlations between Fe2 sites on different ladders are stronger than those between the Fe1 sites on different chains in the $\gamma_{HS} = 1/6$ plateau. These transverse correlations result in four new Bragg peaks in the structure factor, Fig. 6b and 7b, which are accurately reproduced by the effective model (eqn (9)), Fig. 6e and 7b.

In the 2/3 plateau with two types of Fe2 site ($\Delta H_{2a} > \Delta H_{2b} > \Delta H_1$; Fig. 3c) the Fe1 and Fe2b sites are almost all HS, and the Fe2a are almost all LS, Fig. 4b. This corresponds to the phase depicted in Fig. 5c. This can be understood straightforwardly as driven by the crystallographically distinct Fe sites without needing the elastic interactions to drive the long-range spin state order. However, the elastic interactions are necessary to drive the change of spin state into a true thermodynamic phase transition rather than a crossover. Furthermore, the elastic interactions still renormalise $T_{2/3} \to T^*_{2/3}$ in a similar fashion to that described above of three inequivalent Fe sites.

In the 5/6 plateau, Fig. 4c, the Fe1 and Fe2b sites are almost all HS. Thus, we can understand the behaviour of the Fe2a sites by considering the case where all of the Fe1 and Fe2b sites are HS. This allows us to derive an effective Hamiltonian for the Fe2a sites from the full Hamiltonian (eqn (2)) by setting $\sigma_i = 1$ for all Fe1 and Fe2b sites, yielding

$$\begin{aligned} H_{5/6} &= \frac{1}{2}\left[6J_1 + 8J_2 + 4J_3 + 10J_4 + 2J_5 - \frac{8}{3}J_\infty + \Delta H_{2a} - T\Delta S\right] \sum_{i\in \mathrm{Fe2a}} \sigma_i + J_1 \sum_{\langle i,j\rangle_1 \in \mathrm{Fe2a}} \sigma_i\sigma_j + J_3 \sum_{\langle i,j\rangle_3 \in \mathrm{Fe2a}} \sigma_i\sigma_j \\ &\quad + J_4 \sum_{\langle i,j\rangle_4 \in \mathrm{Fe2a}} \sigma_i\sigma_j + J_5 \sum_{\langle i,j\rangle_5 \in \mathrm{Fe2a}} \sigma_i\sigma_j \\ &\quad - \frac{J_\infty}{N} \sum_{i,j\in \mathrm{Fe2a}} \sigma_i\sigma_j. \end{aligned} \tag{11}$$

This describes antiferroelastically coupled nearest neighbour dimers ($J_1 > 0$), which favours pairs of HS and LS SCO centres, with weaker, longer range, interaction coupling the dimers, Fig. 5b. Thus, we now have a q0d model.

As we now expect, the effective q0d model of the 5/6 plateau (eqn (11)) predicts significant renormalisation of $T_{5/6}$:

$$\begin{aligned} T^*_{5/6} &= \frac{\left(6J_1 + 8J_2 + 4J_3 + 10J_4 + 2J_5 - \frac{8}{3}J_\infty\right) + \Delta H_{2a}}{\Delta S} \\ &= T_{5/6} - \frac{2(7k_1 + 8k_2 + 40k_3 + 85k_4 + 104k_5)\delta^2}{3\Delta S} \end{aligned} \tag{12}$$

So elastic interactions decrease $T_{5/6}$. For the parameters used in Fig. 3c $T_{5/6} \simeq 3.57|k_1|\delta^2/k_B$ whereas $T^*_{5/6} \simeq 2.46|k_1|\delta^2/k_B$. Again, this simple theory is in good agreement with our Monte Carlo results, Fig. 3c.

The truncated two point spin state correlation function reveals short range correlations between Fe2a sites, Fig. 8d, but no significant correlations between Fe2a sites and either Fe1 or Fe2b sites, Fig. 8e and f. Again, the presence of only weak short range correlations means that there is no well defined diffuse scattering pattern in the structure factor, Fig. 6c. Indeed, the structure factor calculated analytically assuming no correlations between Fe2a sites and the rest of the lattice,

Fig. 6f, is in good agreement with the Monte Carlo simulation, Fig. 7c.

Thus three phases described above, namely the 1/6, 2/3 and 5/6 plateau, show disordered phases without long range spin state order and with extremely weak short range correlations. In each phase the structure factors are similar to those of long range spin state ordered phases. In particular none of the phases show well defined patterns of diffuse scattering.

3.2 Diffuse scattering from quasi-one-dimensional spin crossover chains

We do not observe well defined diffuse scattering in the previous section because in all cases the short-range correlations are extremely weak. This is in large part due to the emergent q1d and q0d descriptions and the weak interchain/interdimer interaction. However, sufficiently strong short-range correlations can give rise to diffuse scattering when there is reduced dimensionality. To show this we now report the results of Monte Carlo simulations for a different set of parameters: $k_1 < 0$, $k_2 = 1.6|k_1|$, $k_3 = k_4 = k_5 = 0$, $\overline{\Delta H} = 18|k_1|\delta^2$, $\delta H_1 = 17|k_1|\delta^2$, $\delta H_2 = 0|k_1|\delta^2$, $\Delta S = 4\ln(5)k_B$; Fig. 9.

The Monte Carlo simulation shows two intermediate plateaus, one at $\gamma_{HS} = 1/6$ and the other at $\gamma_{HS} = 2/3$, Fig. 9a. The spin state ordering at $\gamma_{HS} = 1/6$ is the same as in the previous simulation (Fig. 5e), while at $\gamma_{HS} = 2/3$ we observe a mixture of the two spin state orderings depicted in Fig. 5c and d (and states related by symmetry).

The large value of k_2 in this simulation causes strong intrachain correlations in the $\gamma_{HS} = 1/6$ plateau. The two-point spin state correlation function between Fe1 sites, Fig. 9c, shows much stronger and longer-ranged correlations than in the simulation described above, Fig. 8a. This leads to a clear pattern of diffuse scattering in structure factor, Fig. 9b. The integral over the first Brillouin zone of this structure factor is in reasonable agreement with the predictions of the effective q1d model (eqn (5)), Fig. 9d, although the latter slightly underestimates the diffuse scatter. This underlines that in order to get experimentally detectable diffuse scattering it is necessary to have strong short-range correlations in the disordered state, and in particular, that the range of the correlations should be significantly longer than a lattice constant.

It is interesting to compare these results to the behaviour observed by Neville, *et al.* for three analogous 1D polymeric iron(II) SCO materials that contain the ligand 4,6-bis(2′,2″-pyridyl)pyrazine.[17] They observed diffuse scattering planes between Bragg peaks in X-ray diffraction measurements. Neville, *et al.* interpreted this as HS–LS–HS–LS ordering along 1D chains, and random spin state ordering between adjacent chains.

In our simulations the Fe1 sites along the chains have a 50% chance of either being HS or LS, but display strong short-range correlations with adjacent sites tending to have opposite pseudo-spins (HS–LS), as indicated by the two-point correlation: $g_{ij} \simeq -1$ for nearest neighbours (Fig. 9c). However, we find much weaker correlations between chains, resulting in planes

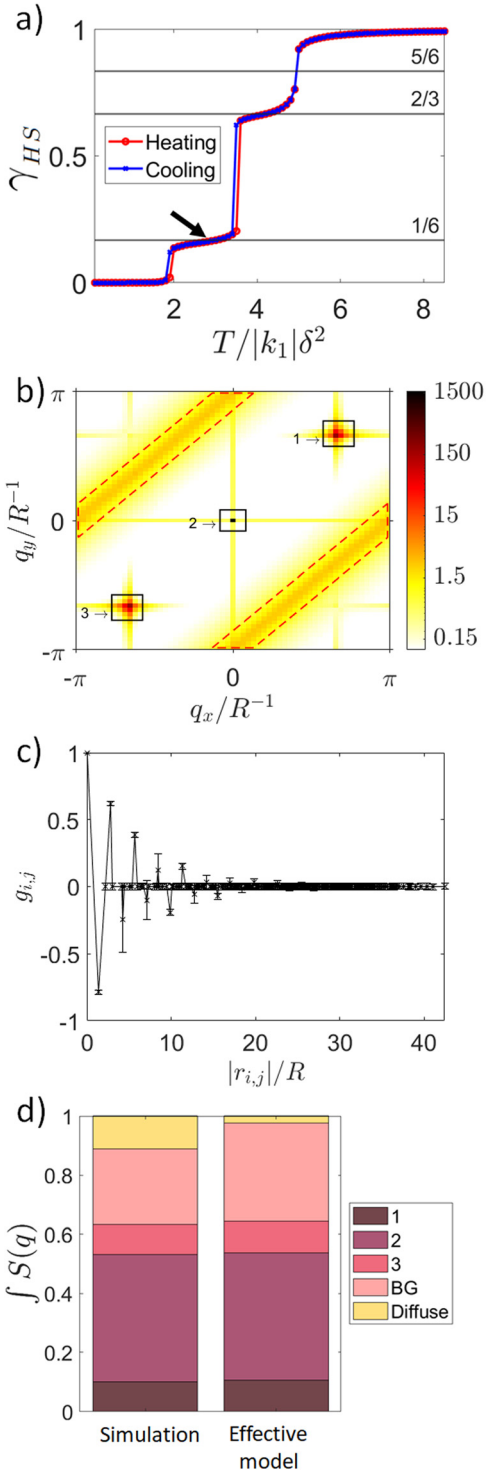

Fig. 9 Strong short-range correlations lead to well defined patterns in the diffuse scattering. (a) Calculated fraction of HS metals, the black arrow indicates the temperature, $T = 3.0|k_1|\delta^2$, at which panels (b)–(d) where calculated. (b) Structure factor, $S(\boldsymbol{q})$, the red dashed parallelograms enclose the areas where diffuse scattering is observed. (c) The two-point spin state correlation function as a function of separation $|r_{i,j}|$ between Fe1 sites shows stronger and longer-ranged correlations than are observed in 8a. (d) Bar plot representing the integral over the first Brillouin zone of the structure factor in (b), "Diffuse" indicates the integral over the area enclosed by the red dashed parallelograms. For this simulation we take $k_1 < 0$, $k_2 = 1.6|k_1|$, $k_3 = k_4 = k_5 = 0$, $\overline{\Delta H} = 18|k_1|\delta^2$, $\delta H_1 = 17|k_1|\delta^2$, $\delta H_2 = 0|k_1|\delta^2$, $\Delta S = 4\ln(5)k_B$.

of diffuse scatter between Bragg peaks in the structure factor 9b. Thus, while the current model is clearly not appropriate for these materials, our results show that strong short-range correlations, rather than long-range spin state order, could also explain Neville *et al.*'s experiments.[17]

4 Conclusions

We have identified a route by which multistep transitions can emerge in spin crossover materials without long-range spin state order of the spin states, as observed experimentally in the SCO compound $[Fe^{II}_3(saltrz)_6(M^{II}(CN)_4)_3]\cdot 8(H_2O)$, where M^{II} = Pd, Pt, and saltrz = (*E*)-2-((((4*H*-1,2,4-triazol-4-yl)imino)methyl)phenol).[16] We demonstrated that intermediate plateaus can emerge from the interplay between the local physics of the SCO centres (ΔH_n) and the elastic interactions (k_i). This interplay can reduce the effective dimensionality of the model to q0d or q1d. Reduced dimensionality leads naturally to highly disordered states at non-zero temperatures. It is interesting to note that similar mechanisms have also been proposed for the origin of quantum disorder in spin liquids.[61–80]

We found that disordered phases with weak short-range correlations produce structure factors that are similar to those of long range spin state ordered phases, which can complicate their experimental identification. Diffuse scattering is only observed when strong short-range correlations are present. In other parameter regimes of our model we find diffuse scattering, and we used this to propose an alternative explanation of the diffuse scattering observed by Neville, *et al.* in three 4,6-bis(2′,2″-pyridyl)pyrazine based SCO polymers that does not require long-range spin state order. Measurement of the PDF would provide a powerful tool to further analyse and distinguish disordered phases, as it provides the same information as the spin state correlation functions calculated above.

Author contributions

GR: conceptualization, data curation, formal analysis, investigation, methodology, software, visualization, writing – original draft. JC: conceptualization, methodology, supervision. BJP: conceptualization, funding acquisition, methodology, project administration, supervision, writing – review & editing.

Conflicts of interest

There are no conflicts to declare.

Acknowledgements

We thank Oliver Bellwood, Cameron Kepert, Ross McKenzie, and Suzanne Neville for helpful conversations. This work was supported by the Australian Research Council through project DP200100305.

References

1 A. Simonov and A. L. Goodwin, *Nat. Rev. Chem.*, 2020, **4**, 657–673.
2 B. Wehinger, D. Chernyshov, M. Krisch, S. Bulat, V. Ezhov and A. Bosak, *J. Phys.: Condens. Matter*, 2014, **26**, 265401.
3 C. L. Henley, *Annu. Rev. Condens. Matter Phys.*, 2010, **1**, 179–210.
4 T. Fennell, P. P. Deen, A. R. Wildes, K. Schmalzl, D. Prabhakaran, A. T. Boothroyd, R. J. Aldus, D. F. McMorrow and S. T. Bramwell, *Science*, 2009, **326**, 415–417.
5 D. J. P. Morris, D. A. Tennant, S. A. Grigera, B. Klemke, C. Castelnovo, R. Moessner, C. Czternasty, M. Meissner, K. C. Rule, J.-U. Hoffmann, K. Kiefer, S. Gerischer, D. Slobinsky and R. S. Perry, *Science*, 2009, **326**, 411–414.
6 J. Cruddas and B. J. Powell, *J. Am. Chem. Soc.*, 2019, **141**, 19790–19799.
7 J. Cruddas and B. J. Powell, *Phys. Rev. B*, 2021, **104**, 024433.
8 I. Gudyma and V. Yarema, *Appl. Nanosci.*, 2023, **13**, 6719–6726.
9 J. Cruddas, G. Ruzzi and B. J. Powell, *J. Appl. Phys.*, 2021, **129**, 185102.
10 S. Pillet, *J. Appl. Phys.*, 2021, **129**, 181101.
11 H. Watanabe, K. Tanaka, N. Bréfuel, H. Cailleau, J.-F. Létard, S. Ravy, P. Fertey, M. Nishino, S. Miyashita and E. Collet, *Phys. Rev. B*, 2016, **93**, 014419.
12 E. Collet, H. Watanabe, N. Bréfuel, L. Palatinus, L. Roudaut, L. Toupet, K. Tanaka, J.-P. Tuchagues, P. Fertey, S. Ravy, B. Toudic and H. Cailleau, *Phys. Rev. Lett.*, 2012, **109**, 257206.
13 C. Mariette, E. Trzop, S. Zerdane, P. Fertey, D. Zhang, F. J. Valverde-Muñoz, J.-A. Real and E. Collet, *Acta Crystallogr., Sect. B: Struct. Sci., Cryst. Eng. Mater.*, 2017, **73**, 660–668.
14 E. Collet and P. Guionneau, *C. R. Chim.*, 2018, **21**, 1133–1151.
15 C. Bressler, W. Gawelda, A. Galler, M. M. Nielsen, V. Sundström, G. Doumy, A. M. March, S. H. Southworth, L. Young and G. Vankó, *Faraday Discuss.*, 2014, **171**, 169–178.
16 N. F. Sciortino, K. A. Zenere, M. E. Corrigan, G. J. Halder, G. Chastanet, J.-F. Létard, C. J. Kepert and S. M. Neville, *Chem. Sci.*, 2017, **8**, 701–707.
17 S. M. Neville, B. A. Leita, G. J. Halder, C. J. Kepert, B. Moubaraki, J.-F. Létard and K. S. Murray, *Chem. – Eur. J.*, 2008, **14**, 10123–10133.
18 A. Bousseksou, F. Varret and J. Nasser, *J. Phys. I*, 1993, **3**, 1463–1473.
19 J. Cruddas and B. J. Powell, *Inorg. Chem. Front.*, 2020, **7**, 4424–4437.
20 M. Paez-Espejo, M. Sy and K. Boukheddaden, *J. Am. Chem. Soc.*, 2016, **138**, 3202–3210.
21 G. Azzolina, R. Bertoni and E. Collet, *J. Appl. Phys.*, 2021, **129**, 085106.
22 N. F. Sciortino, F. Ragon, Y. M. Klein, C. E. Housecroft, C. G. Davies, G. N. L. Jameson, G. Chastanet and S. M. Neville, *Inorg. Chem.*, 2018, **57**, 11068–11076.
23 N. Ortega-Villar, M. Muñoz and J. Real, *Magnetochemistry*, 2016, **2**, 16.

24 C.-J. Zhang, K.-T. Lian, S.-G. Wu, G.-Z. Huang, Z.-P. Ni and M.-L. Tong, *Inorg. Chem. Front.*, 2020, **4**, 911.
25 C.-J. Zhang, K.-T. Lian, G.-Z. Huang, S. Bala, Z.-P. Ni and M.-L. Tong, *Chem. Commun.*, 2019, **55**, 11033.
26 Y. Meng, Q. Sheng, M. N. Hoque, Y. Chen, S. Wu, J. Tucek, R. Zboril, T. Liu, Z. Ni and M. Tong, *Chem. – Eur. J.*, 2017, **23**, 10034.
27 J. E. Clements, J. R. Price, S. M. Neville and C. J. Kepert, *Angew. Chem., Int. Ed.*, 2016, **55**, 15105–15109.
28 G. Agustí, A. B. Gaspar, M. C. Muñoz, P. G. Lacroix and J. A. Real, *Aust. J. Chem.*, 2009, **62**, 1155.
29 K. Takashi, K.-T. Chihiro, K. Chikahide, S. Toshiaki and K. Takafumi, *Chem. Lett.*, 2008, **37**, 422.
30 G. Agustí, M. C. Muñoz, A. B. Gaspar and J. A. Real, *Inorg. Chem.*, 2008, **47**, 2552.
31 N. F. Sciortino, K. R. Scherl-Gruenwald, G. Chastanet, G. J. Halder, K. W. Chapman, J.-F. Létard and C. J. Kepert, *Angew. Chem., Int. Ed.*, 2012, **51**, 10154–10158.
32 F.-L. Liu, D. Li, L.-J. Su and J. Tao, *Dalton Trans.*, 2018, **47**, 1407–1411.
33 M. J. Murphy, K. A. Zenere, F. Ragon, P. D. Southon, C. J. Kepert and S. M. Neville, *J. Am. Chem. Soc.*, 2017, **139**, 1330–1335.
34 K. A. Zenere, S. G. Duyker, E. Trzop, E. Collet, B. Chan, P. W. Doheny, C. J. Kepert and S. M. Neville, *Chem. Sci.*, 2018, **9**, 5623–5629.
35 E. Milin, V. Patinec, S. Triki, E.-E. Bendeif, S. Pillet, M. Marchivie, G. Chastanet and K. Boukheddaden, *Inorg. Chem.*, 2016, **55**, 11652–11661.
36 L. Piñeiro-López, M. Seredyuk, M. C. Muñoz and J. A. Real, *Chem. Commun.*, 2014, **50**, 1833–1835.
37 F.-L. Liu and J. Tao, *Chem. – Eur. J.*, 2017, **23**, 18252–18257.
38 Y. M. Klein, N. F. Sciortino, F. Ragon, C. E. Housecroft, C. J. Kepert and S. M. Neville, *Chem. Commun.*, 2014, **50**, 3838–3840.
39 V. A. Money, C. Carbonera, J. Elhaïk, M. A. Halcrow, J. A. K. Howard and J.-F. Létard, *Chem. – Eur. J.*, 2007, **13**, 5503–5514.
40 A. J. Fitzpatrick, E. Trzop, H. Müller-Bunz, M. M. DÃ®rtu, Y. Garcia, E. Collet and G. G. Morgan, *Chem. Commun.*, 2015, **51**, 17540–17543.
41 J. Klingele, D. Kaase, M. H. Klingele, J. Lach and S. Demeshko, *Dalton Trans.*, 2010, **39**, 1689–1691.
42 D. Chernyshov, M. Hostettler, K. W. Törnroos and H.-B. Bürgi, *Angew. Chem., Int. Ed.*, 2003, **42**, 3825–3830.
43 B. J. C. Vieira, J. T. Coutinho, I. C. Santos, L. C. J. Pereira, J. C. Waerenborgh and V. da Gama, *Inorg. Chem.*, 2013, **52**, 3845–3850.
44 H. Hang, B. Fei, X. Q. Chen, M. L. Tong, V. Ksenofontov, I. A. Gural'skiy and X. Bao, *J. Mater. Chem. C*, 2018, **6**, 3352–3361.
45 J.-B. Lin, W. Xue, B.-Y. Wang, J. Tao, W.-X. Zhang, J.-P. Zhang and X.-M. Chen, *Inorg. Chem.*, 2012, **51**, 9423.
46 G. J. Halder, C. J. Kepert, B. Moubaraki, K. S. Murray and J. D. Cashion, *Science*, 2002, **298**, 1762–1765.
47 G. J. Halder, K. W. Chapman, S. M. Neville, B. Moubaraki, K. S. Murray, J.-F. Létard and C. J. Kepert, *J. Am. Chem. Soc.*, 2008, **130**, 17552.
48 X. Bao, P.-H. Guo, W. Liu, J. Tucek, W.-X. Zhang, J.-D. Leng, X.-M. Chen, I. A. Gural'skiy, L. Salmon, A. Bousseksou and M.-L. Tong, *Chem. Sci.*, 2012, **3**, 1629.
49 C. J. Adams, M. C. Muñoz, R. E. Waddington and J. A. Real, *Inorg. Chem.*, 2011, **50**, 10633.
50 W. Liu, Y.-Y. Peng, S.-G. Wu, Y.-C. Chen, M. N. Hoque, Z.-P. Ni, X.-M. Chen and M.-L. Tong, *Angew. Chem., Int. Ed.*, 2017, **56**, 14982.
51 N. Ortega-Villar, M. C. Muñoz and J. A. Real, *Magnetochemistry*, 2016, **2**, 16.
52 K. D. Murnaghan, C. Carbonera, L. Toupet, M. Griffin, M. M. DÃ®rtu, C. Desplanches, Y. Garcia, E. Collet, J.-F. Létard and G. G. Morgan, *Chem. – Eur. J.*, 2014, **20**, 5613–5618.
53 J. Luan, J. Zhou, Z. Liu, B. Zhu, H. Wang, X. Bao, W. Liu, M.-L. Tong, G. Peng, H. Peng, L. Salmon and A. Bousseksou, *Inorg. Chem.*, 2015, **54**, 5145–5147.
54 Z.-Y. Li, H. Ohtsu, T. Kojima, J.-W. Dai, T. Yoshida, B. K. Breedlove, W.-X. Zhang, H. Iguchi, O. Sato, M. Kawano and M. Yamashita, *Angew. Chem., Int. Ed.*, 2016, **55**, 5184–5189.
55 N. Bréfuel, H. Watanabe, L. Toupet, J. Come, N. Matsumoto, E. Collet, K. Tanaka and J.-P. Tuchagues, *Angew. Chem., Int. Ed.*, 2009, **48**, 9304–9307.
56 S. M. Neville, private communication.
57 A. Bunde, *Phys. Lett. A*, 1974, **47**, 483–484.
58 H. J. Monkhorst and J. D. Pack, *Phys. Rev. B: Solid State*, 1976, **13**, 5188–5192.
59 M. Plischke and B. Bergersen, *Equilibrium Statistical Physics*, World Scientific, 2006.
60 M. W. Terban and S. J. L. Billinge, *Chem. Rev.*, 2022, **122**, 1208–1272.
61 B. J. Powell and R. H. McKenzie, *Phys. Rev. Lett.*, 2007, **98**, 027005.
62 Y. Hayashi and M. Ogata, *J. Phys. Soc. Jpn.*, 2007, **76**, 053705.
63 M. Kohno, O. A. Starykh and L. Balents, *Nat. Phys.*, 2007, **3**, 790–795.
64 L. Balents, *Nature*, 2010, **464**, 199–208.
65 B. J. Powell, E. P. Kenny and J. Merino, *Phys. Rev. Lett.*, 2017, **119**, 087204.
66 E. P. Kenny, A. C. Jacko and B. J. Powell, *Angew. Chem., Int. Ed.*, 2019, **58**, 15082–15088.
67 E. P. Kenny, G. David, N. Ferré, A. C. Jacko and B. J. Powell, *Phys. Rev. Mater.*, 2020, **4**, 044403.
68 A. C. Jacko and B. J. Powell, *Phys. Chem. Chem. Phys.*, 2021, **23**, 5012–5019.
69 C. Dissanayake, A. C. Jacko, K. Kumarasinghe, R. Munir, H. Siddiquee, W. J. Newsome, F. J. Uribe-Romo, E. S. Choi, S. Yadav, X.-Z. Hu, Y. Takano, S. Pakhira, D. C. Johnston, Q.-P. Ding, Y. Furukawa, B. J. Powell and Y. Nakajima, *Phys. Rev. B*, 2023, **108**, 134418.
70 Y. Choi, S. Lee, J.-H. Lee, S. Lee, M.-J. Seong and K.-Y. Choi, *Nat. Commun.*, 2021, **12**, 1–8.
71 S. A. Zvyagin, A. N. Ponomaryov, J. Wosnitza, D. Hirai, Z. Hiroi, M. Gen, Y. Kohama, A. Matsuo, Y. H. Matsuda and K. Kindo, *Nat. Commun.*, 2022, **13**, 6310.

72 G. Cao, H. Zheng, H. Zhao, Y. Ni, C. A. Pocs, Y. Zhang, F. Ye, C. Hoffmann, X. Wang, M. Lee, M. Hermele and I. Kimchi, *npj Quant. Mater.*, 2020, **5**, 26.
73 S. E. Sebastian, N. Harrison, C. D. Batista, L. Balicas, M. Jaime, P. A. Sharma, N. Kawashima and I. R. Fisher, *Nature*, 2006, **441**, 617–620.
74 S.-H. Lee, D. Louca, H. Ueda, S. Park, T. J. Sato, M. Isobe, Y. Ueda, S. Rosenkranz, P. Zschack, J. Íñiguez, Y. Qiu and R. Osborn, *Phys. Rev. Lett.*, 2004, **93**, 156407.
75 R. Okuma, M. Kofu, S. Asai, M. Avdeev, A. Koda, H. Okabe, M. Hiraishi, S. Takeshita, K. M. Kojima, R. Kadono, T. Masuda, K. Nakajima and Z. Hiroi, *Nat. Commun.*, 2021, **12**, 4382.
76 K. Ido, K. Yoshimi, T. Misawa and M. Imada, *npj Quant. Mater.*, 2022, **7**, 48.
77 B. Zhang, Y. Zhang, Z. Wang, D. Wang, P. J. Baker, F. L. Pratt and D. Zhu, *Sci. Rep.*, 2014, **4**, 6451.
78 R. Pohle, N. Shannon and Y. Motome, *Phys. Rev. B*, 2023, **107**, L140403.
79 S. Feng, A. Agarwala and N. Trivedi, *arXiv*, 2023, preprint, arXiv:2308.08116, DOI: **10.48550/arXiv.2308.08116**.
80 O. R. Bellwood, H. L. Nourse and B. J. Powell, Raman scattering signatures of spinons and triplons in frustrated antiferromagnets, *arXiv*, 2024, preprint, arXiv:2401.10452, DOI: **10.48550/arXiv.2401.10452**.